# Time scales for binary processes from light heavy-ion reactions

A. A. P. Suaide, N. Added, N. Aissaoui, E. E. Alonso, W. H. Z. Cárdenas, R. J. Fujii, M. M. de Moura, M. G. Munhoz, F. A. Souza, E. M. Szanto, A. Szanto de Toledo, and N. Carlin

*Instituto de Física, Universidade de São Paulo, Departamento de Física Nuclear, Laboratório Pelletron, Caixa Postal 66318, 05315-970, São Paulo, SP, Brazil*

M. Papa

*INFN, Sezione di Catania, Corso Italia, 57, I-95129, Italy*

(Received 1 March 2002; published 17 July 2002)

Binary decay excitation functions have been measured for the $^{16}O+^{10}B$ system at 22 MeV $<E_{c.m.}<24.5$ MeV ($\delta E_{c.m.}\sim 20$ keV) and 17 MeV$<E_{c.m.}<25$ MeV ($\delta E_{c.m.}\sim 190$ keV) and for the $^{19}F+^{12}C$ system at 22 MeV$<E_{c.m.}<24.5$ MeV ($\delta E_{c.m.}\sim 20$ keV). The binary fragments were identified by the kinematic coincidence technique. The excitation functions for these systems show strong fluctuations and average decay widths were obtained through the analysis of energy correlation functions. The small widths observed for the $^{16}O+^{10}B$ (about 20 keV) and $^{19}F+^{12}C$ (about 40 keV) systems show a constant behavior with the fragments' excitation energy and scattering angle. These widths correspond to an intermediate system time scale of about $2\times10^{-20}$ s, which is larger than its revolution time. These features suggest the presence of the fusion-fission mechanism, where the compound nucleus takes a long time to acquire a relaxed shape and thermal equilibrium. For the $^{16}O+^{10}B$ system, larger widths (about 350 keV) were also observed, which are related to a faster process. These widths show a clear dependence with the scattering angle in the elastic scattering channel. These aspects are expected for a process where the time scale is comparable to the intermediate system revolution time, like an orbiting mechanism. Theoretical predictions for fusion-fission and orbiting mechanisms were compared to the experimental results and a good agreement was observed.

DOI: 10.1103/PhysRevC.66.014607 PACS number(s): 24.60.−k, 25.70.Gh, 25.70.Jj

## I. INTRODUCTION

In the last years, a large number of experimental evidences for binary decay of light nuclear systems have been collected [1–8]. These evidences were first noticed in the elastic scattering angular distribution of $\alpha$-particle-like systems that show a strange behavior at very large scattering angles [anomalous large angle scattering (ALAS)] [9] and it was first explained as an elastic transfer between target and projectile [10]. On the other hand, these phenomena were also observed for very high mass asymmetric systems, which suggests another reaction mechanism besides the elastic transfer. The ALAS phenomenon could be explained by the presence of the ''orbiting'' mechanism that consists of the formation and decay into the elastic channel of a dinuclear complex system [11,12]. This mechanism is similar to the deep inelastic collision (DIC) for heavier systems and higher energies. One of the orbiting mechanism characteristics is the isotropic angular distribution, $d\sigma/d\theta_{c.m.}$. This fact suggests that the dinuclear system is bound for a time comparable or larger than its rotation time, which allows the participant nuclei to exchange part of their mass. Because of the high angular momentum, the binary emission in this mechanism is enhanced when compared to light particle emission. On the other hand, this time scale is not sufficient for a complete equilibration and the decay yields are strongly dependent on the entrance channel [1,2,13–16]. These characteristics were also observed for systems without the $\alpha$-particle-like structure, such as $^{16,17,18}O+^{10,11}B$, $^{19}F+^{9}Be$, $^{35}Cl+^{12}C$, and $^{31}P+^{16}O$ [3,4,17,18]. But, in this case, the binary emission of the intermediate system does not depend on the way the intermediate system is formed, which suggests the formation of an equilibrated intermediate system, such as a compound nucleus, the experimental results being well explained within a fusion-fission context [3]. The main characteristics of the mechanisms above suggest different time evolutions and time scale measurements could be a suitable way to study the dynamics of these mechanisms.

There are many techniques to investigate reaction time scales. In this work we concentrate on the cross section statistical fluctuations. When an intermediate system is formed at high excitation energy, the average level widths are larger than the separation between them. In this situation it is not possible to separate these levels and the cross section is strongly dominated by resonances, which can interfere with each other. This interference is random, and gives rise to fluctuations in the cross section. The average fluctuation widths are related to the average level width ($\Gamma$) of the intermediate system, which is related to the mean lifetime ($\tau$) through the uncertainty principle. These fluctuations were theoretically explained for the first time by Ericson [19,20] in the framework of a compound nucleus formation. In the last years these fluctuations have been also observed in DIC [21–25]. Recently, the partially overlapping molecular level model (POMLM) [25–27] has been developed to take into account the main characteristics of the fluctuations observed in DIC.

In this work we investigate the cross section fluctuations for binary decay channels of the $^{16}O+^{10}B$ and $^{19}F+^{12}C$ systems. These fluctuations were analyzed in terms of the sta-

 

TABLE I. Energy range measured in this work for the $^{16}O + ^{10}B$ and $^{19}F + ^{12}C$ systems. $E_{lab}$ and $\Delta E_{lab}$ are the energy range and step in the laboratory frame and $E_{c.m.}$ and $\Delta E_{c.m.}$ are the energy range and step in the center-of-mass frame.

| System | $E_{lab}$ (MeV) | $\Delta E_{lab}$ (MeV) | $E_{c.m.}$ (MeV) | $\Delta E_{c.m.}$ (MeV) |
|---|---|---|---|---|
| $^{16}O + ^{10}B$ | $57 < E < 64$ | $\sim 60$ | $22 < E < 24$ | $\sim 23$ |
| $^{16}O + ^{10}B$ | $44 < E < 65$ | $\sim 500$ | $17 < E < 25$ | $\sim 190$ |
| $^{19}F + ^{12}C$ | $57 < E < 64$ | $\sim 70$ | $22 < E < 24$ | $\sim 27$ |

tistical theory and the results were compared to model predictions for compound nuclei and dinuclear systems' formation. This paper is organized as follows. The experimental setup and data reduction is briefly described in Sec. II. The results, discussions, and model predictions are presented in Sec. III. The conclusions are presented in Sec. IV.

## II. EXPERIMENTAL SETUP AND DATA REDUCTION

The experiments have been performed for the $^{16}O + ^{10}B$ and $^{19}F + ^{12}C$ systems (see Table I for details about the measured energy range) at the University of São Paulo Pelletron Laboratory. The $^{16}O$ and $^{19}F$ beams were extracted using a SNICS (Source of Negative Ions by Celsium Sputtering) ion source. The targets consisted of self-supporting $^{10}B$ and $^{12}C$ foils of areal densities between 8 and 20 $\mu g/cm^2$ for the case of small energy step measurements ($\delta E_{lab} \sim 60$ keV) and areal densities between 40 and 60 $\mu g/cm^2$ for the case of large energy step measurements ($\delta E_{lab} \sim 500$ keV). A small quantity of gold ($\sim 1-2$ $\mu g/cm^2$) was evaporated on the target surface in order to allow normalization of the experimental cross sections. The main contaminants present in the targets were found to be $^{16}O$, $^{28}Si$, and $^{56}Fe$. The relative thicknesses of these contaminants were obtained using the elastic scattering yield at very small angles and turned out to be less than 1% of the total thickness of the target. The beam energy resolution, considering both the accelerator resolution and energy straggling on the target, was about 50 keV for the thin targets and 150 keV for the thick ones (in the laboratory frame). The carbon buildup was checked using small angle elastic scattering excitation functions and the targets were periodically changed to minimize this effect.

In order to vary the beam energy in small steps, a special target support was built where it is possible to apply high voltage ($-100$ kV$< V <$100 kV), as seen in Fig. 1. With this technique, the beam energy can be varied in small steps avoiding uncertainties related to the hysteresis cycle of the analyzing magnet.

The experimental setup consisted of four $\Delta E$-$E$ telescopes [28] composed by an ionization chamber, to measure the energy loss, and a silicon detector, to measure the residual energy of the incident particle. It is possible to identify the atomic number ($Z$) of the particles with a resolution of $\delta Z/Z \sim 5\%$ up to $Z = 13$. The telescopes were positioned from 10 to 40 deg with respect to the beam direction with an angular spacing of 10 deg. Each telescope has a solid angle coverage of $\Delta\Omega \sim 8$ msr. Moreover, two silicon position sensitive detectors (PSD) were positioned at $-30$ and $-60$ deg to perform coincidence measurements with any $\Delta E$-$E$ detector. A photo of the experimental setup is shown in Fig. 1. A typical $\Delta E$-$E$ spectrum is shown in Fig. 2(a). Using two-body kinematic calculations it is possible to identify the particles from binary processes by selecting events with reconstructed mass of the fragments $A_1$ and $A_2$ in such a way that $A_1 + A_2 = A_{target} + A_{beam}$. This selection removes any systematic uncertainty due to contamination in the target because the reconstructed mass resolution is good enough to discriminate between the reaction on the target and contaminants. A typical $A_1$ versus $A_2$ spectrum for the $^{16}O + ^{10}B$ system is shown in Fig. 2(b).

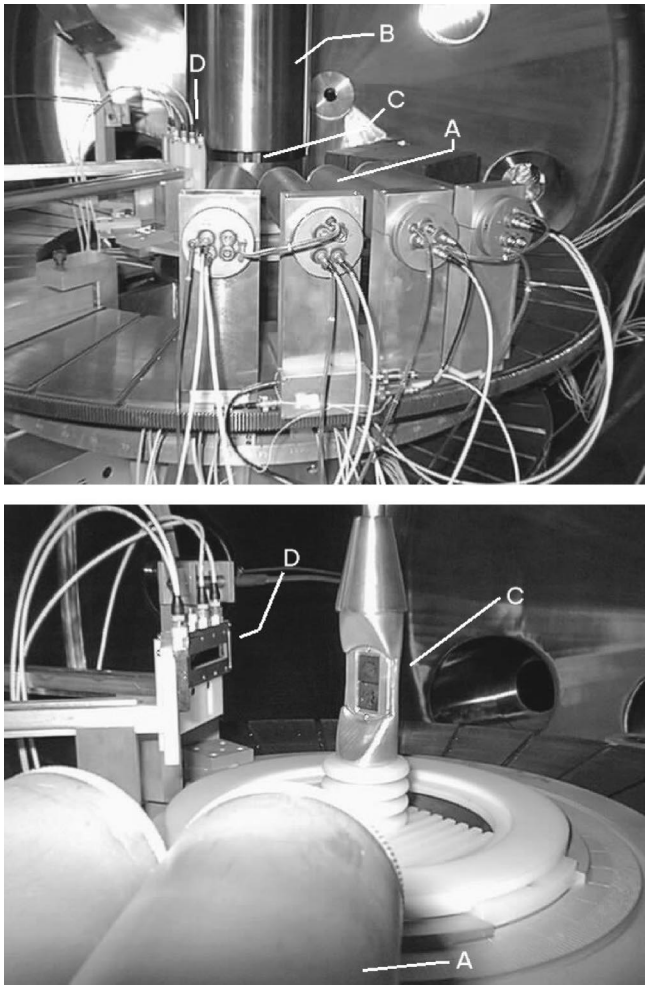


FIG. 1. Photos of the experimental setup. *A* represent the telescopes, *B* represents eletrical shield used to protect the detectors from sparks, *C* is the target support, *D* being the PSD.

One of the excitation energy spectra for binary events is shown in Fig. 3. The continuous line represents the experimental setup efficiency calculated from Monte Carlo simulations, where the experimental geometry, beam spot size, angular and energy stragglings in the target are considered. To obtain the experimental excitation function, the spectra were sliced, in the region where the experimental efficiency is almost constant, in excitation energy intervals of 1 MeV in order to reduce the statistical error bars.

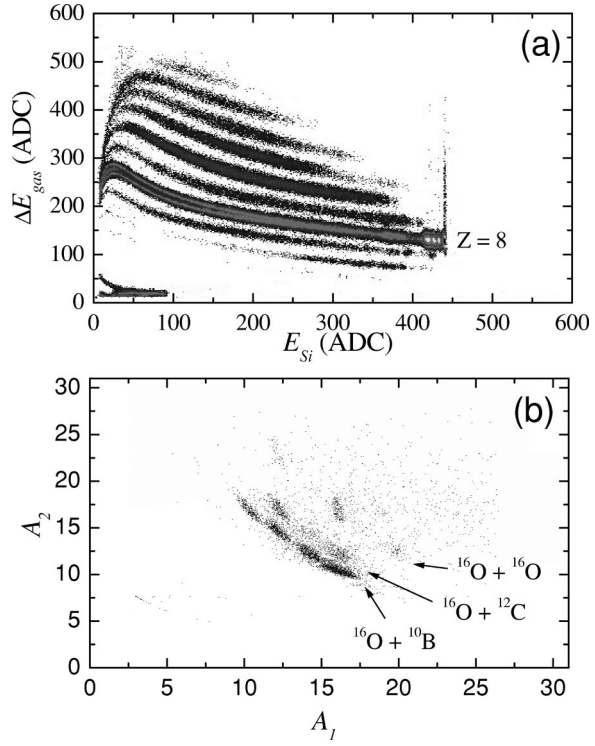


FIG. 2. (a) Typical $\Delta E$-$E$ spectrum for the $^{16}O+^{10}B$ system. (b) Reconstructed mass spectrum for the $^{16}O+^{10}B$ system. It is possible to notice a good separation between the various contaminants in the target.

In this work, the absolute cross section in the center-of-mass frame was obtained by comparison of the yield of the process we are interested in and the yield of the elastic scattering of the projectile by the thin layer of gold deposited in the target. In this case, the cross section for a given process can be written as

$$\frac{d^2\sigma}{d\Omega dE^*} = \frac{Y}{Y_{\mathrm{Au}}}\frac{N_{\mathrm{Au}}}{N}\frac{jac}{jac_{\mathrm{Au}}}\left(\frac{d\sigma}{d\Omega}\right)_{\mathrm{Au}}\frac{1}{f_{eff}}, \tag{1}$$

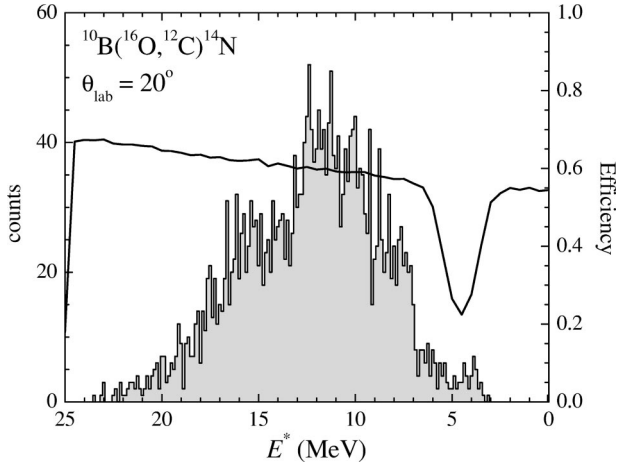


FIG. 3. Typical excitation energy spectrum for binary events. The continuous line represents the experimental setup efficiency calculated from Monte Carlo simulations.

where $Y/Y_{\mathrm{Au}}$ is the relative yield between the process for which we would like to obtain the cross section and the the elastic scattering of the projectile by gold nuclei; $jac$ and $jac_{\mathrm{Au}}$ are the laboratory to center-of-mass frame solid angle transformation for both processes; $(d\sigma/d\Omega)_{\mathrm{Au}}$ is the Rutherford cross section between the projectile and the gold nuclei deposited in the target; $f_{eff}$ is the experimental setup efficiency for a given scattering angle and excitation energy and $N_{\mathrm{Au}}/N$ is the relative thickness between the gold layer deposited in the target and the target itself. In order to obtain the absolute cross section this ratio should be experimentally obtained. In the case of the $^{10}B$ target, once the relative thickness does not change during the data acquisition, this ratio was obtained by a measurement of the elastic scattering at $E_{lab}=12$ MeV. This energy is well below the Coulomb barrier for this system and the absolute cross section is essentially Rutherford. Due to the carbon buildup the relative thickness changes with time in the case of $^{12}C$ target. In this case, the relative thickness was obtained from a measurement of the elastic scattering at a very small angle for each energy and from a comparison to optical model predictions [29]. This measurement was also used to monitor the carbon buildup in the target. The final cross section error bars are composed by the counting statistics and by the experimental uncertainties, such as target thickness, normalization effects, and experimental efficiency and correspond to about 3–7 % of the experimental value. In Fig. 4 we show, for the $^{16}O+^{10}B$ system, a sample of excitation functions for the $^{12}C+^{14}N$ exit channel at different fragment excitation energies. It is possible to notice the presence of strong fluctuations both in the small and large energy step excitation functions. Figure 5 shows excitation functions for different reaction channels and fragments excitation energies for the $^{19}F+^{12}C$ system where strong fluctuations are also observed. These fluctuations will be discussed in detail in the following section. The continuous lines in Figs. 4 and 5 correspond to the average cross section and will also be discussed in the following section.

## III. ANALYSIS AND DISCUSSION

The experimental normalized energy autocorrelation function (NEAF) for a given excitation function was obtained from

$$C_N(\varepsilon,\theta) = C(\varepsilon,\theta)/C(0,\theta), \tag{2}$$

with

$$C(\varepsilon,\theta) = \left\langle \left( \frac{\sigma(E,\theta)}{\langle\sigma(E,\theta)\rangle} - 1 \right) \left( \frac{\sigma(E+\varepsilon,\theta)}{\langle\sigma(E+\varepsilon,\theta)\rangle} - 1 \right) \right\rangle. \tag{3}$$

In the expression above $\sigma(E,\theta)$ is the differential cross section measured at a center-of-mass energy $E$ and center-of-mass angle $\theta$. $\varepsilon$ is the energy increment and the brackets denote energy averages. The energy averaged cross section $\langle\sigma(E,\theta)\rangle$ has been calculated using a polynomial fit. The choice of the polynomial degree should isolate the structures of interest and has been investigated carefully [30]. The decay widths could be obtained directly from the NEAF when

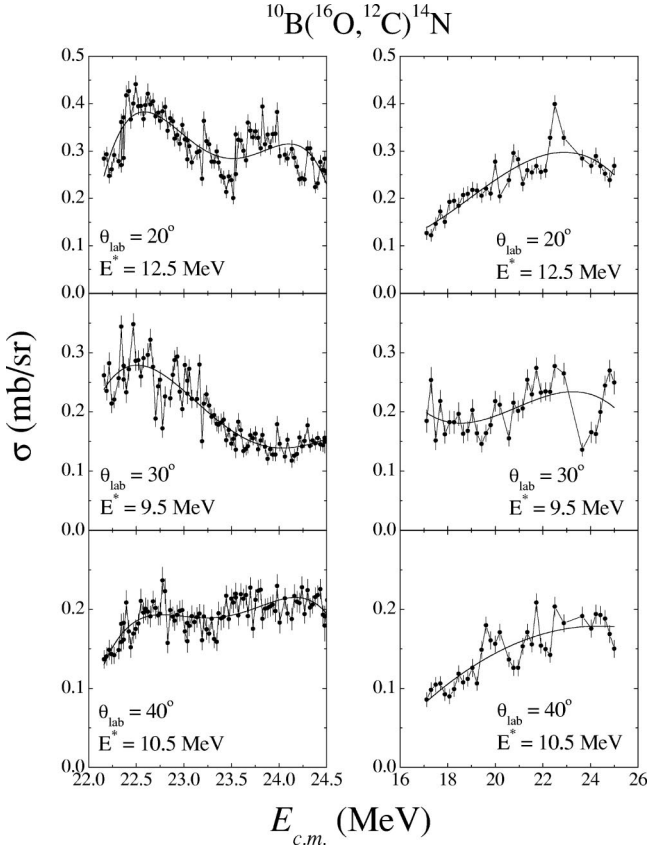


FIG. 4. Typical excitation functions for the $^{16}O+^{10}B$ system corresponding to the $^{12}C+^{14}N$ decay channel for different detection angles and excitation energies and the small (left) and large (right) step measurements. The lines show the averaged cross section used to obtain the NEAF.

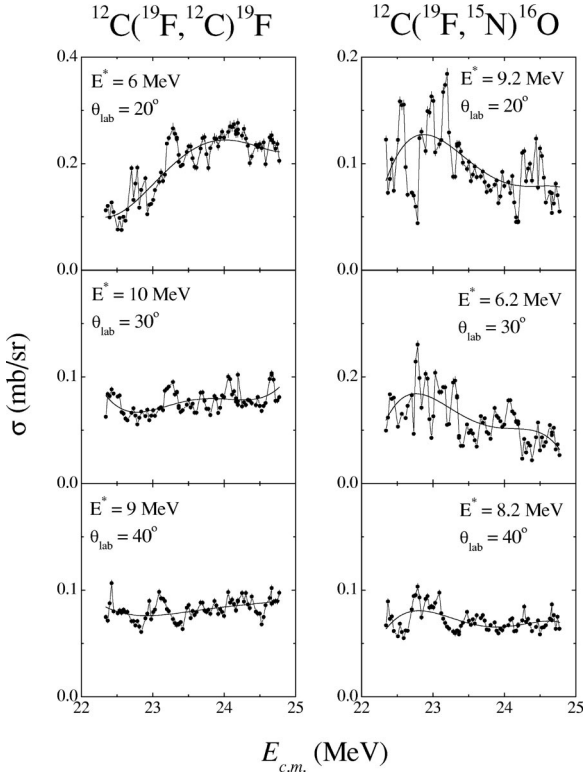


FIG. 5. Typical excitation functions for the $^{19}F+^{12}C$ system relative to the $^{12}C+^{19}F$ (left) and the $^{15}N+^{16}O$ (right) decay channels for different detection angles and excitation energies. The lines show the averaged cross section used to obtain the NEAF.

$C_N(\varepsilon,\theta)$ reaches the value of 0.5. Figures 6–9 show typical NEAF obtained for both measured systems. Solid lines are predictions based on the POMLM and they will be discussed later. The experimental error bars include the contributions due to the statistical counting and the finite range of data (FRD) [30]. This latter error, as can been seen in the figures, manifests itself also through wide oscillations for large values of $\varepsilon$. Typical error bars in the NEAF are about 5–10 % of the experimental value.

### A. Comparison of the data with POMLM

The POMLM is being used to explain the low-density quasimolecular overlapped levels that can generate strong fluctuations in the cross section observed on DIC for heavier systems.

The basic point of this model is the polar expansion of the *S* matrix that connects the initial state $\alpha$ and the final state $\beta$ [27,31–33]. During this expansion, the effect of the coherent rotation of the intermediate state is also taken into account to reproduce the experimental data [25,32,34,35]. The polar expansion is done by considering an overlap of many intermediate states with energy:

$$E_\mu(J)=E_\mu^0+\frac{\hbar^2}{2\,\Im}J(J+1)+i\frac{\Gamma}{2}, \qquad (4)$$

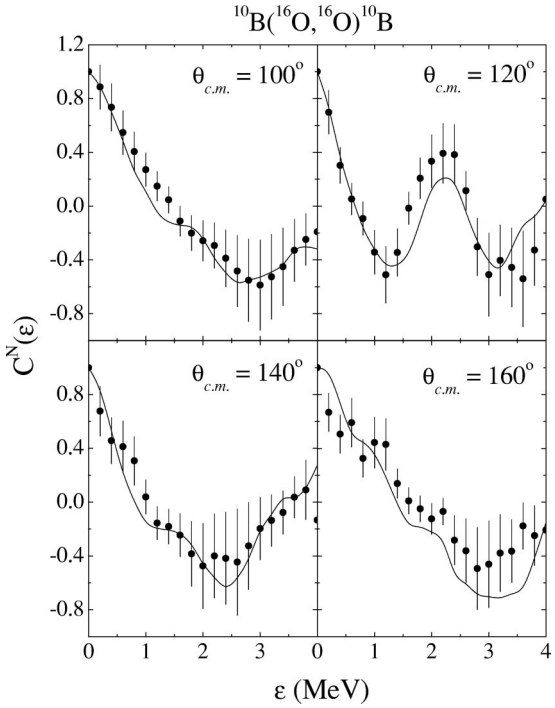


FIG. 6. NEAF for the large step elastic scattering of $^{16}O+^{10}B$ system for different detection angles. The lines show simulations based on POMLM theory with the parameters in Table II.

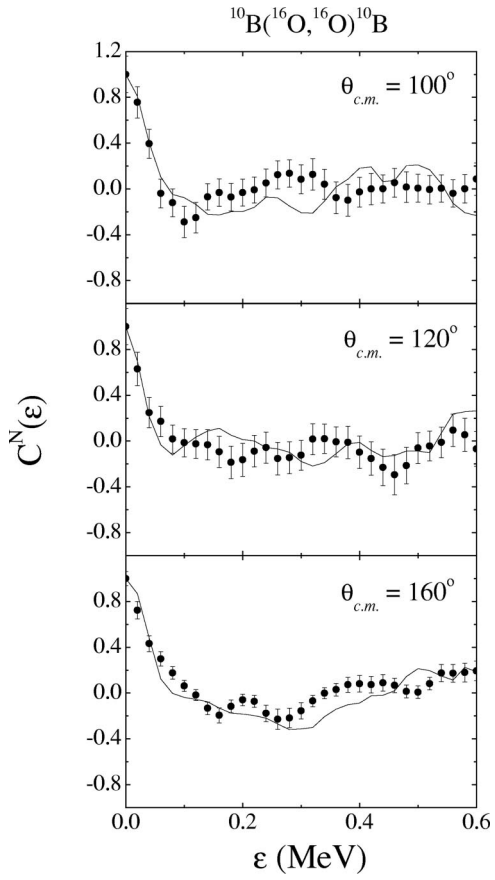


FIG. 7. NEAF for the small step elastic scattering of $^{16}O+^{10}B$ system for different detection angles. The lines show simulations based on POMLM theory with the parameters in Table II.

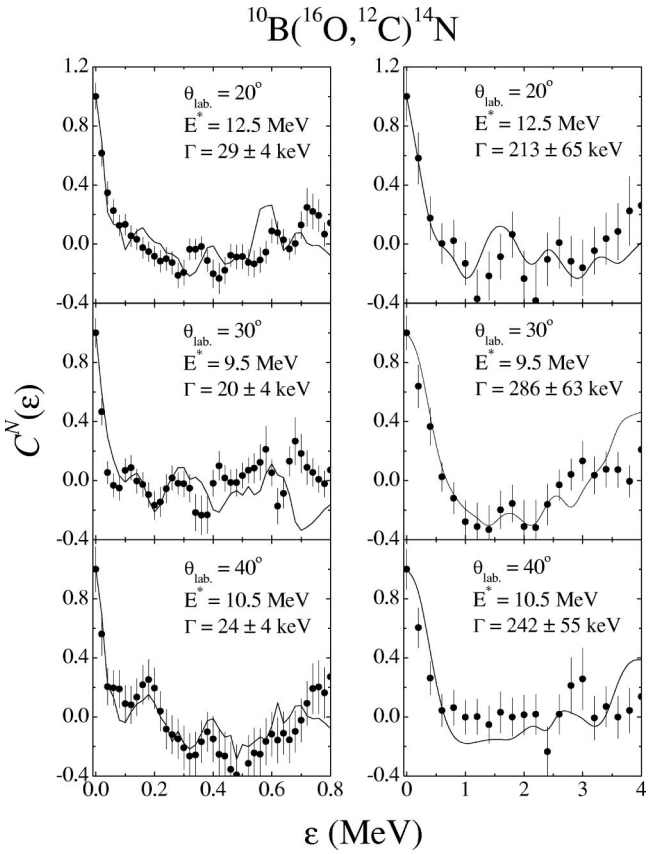


FIG. 8. NEAF for the $^{16}O+^{10}B$ system corresponding to the $^{12}C+^{14}N$ decay channel for different detection angles and excitation energies. Results for the small (left) and large (right) step measurements are shown. The lines show simulations based on POMLM theory with the parameters in Table II.

where $\mathfrak{I}$ is the moment of inertia of the intermediate system and $\Gamma$ is the mean value of the level width. $E_\mu^0$ is the part of the resonant energy that is not connected to the rotational degree of freedom. In this work a sum over a large number of levels is performed. In this case, the resulting cross section for a given energy and angle can be written as

$$\sigma(E,\theta)=\frac{A}{\sin\theta}\sum_{J,J',\mu}(2J+1)(2J'+1)\times[W(J)W(J')]^{1/2}e^{i[\phi(J)-\phi(J')]}\times\frac{P_J(\theta)P_{J'}(\theta)\overline{|b_{\alpha,\mu}|^2}}{[E-E_\mu(J)][E-E_\mu^*(J')]}, \quad (5)$$

where

$$\overline{|b_{\alpha,\mu}|^2}=|\gamma_{\alpha,\mu}|^2\overline{|\gamma_{\mu,\beta}|^2}, \quad (6)$$

$P_J$ is the Legendre polynomial of order $J$, and $W(J)$ is the effective transmition coefficient modeled by a Gaussian centered at $J$ and a standard deviation of $\Delta/\sqrt{2}$. $\phi(J)=\Phi(\overline{J})\times(J-\overline{J})$ is the nonresonant phase shift associated with the scattering amplitude. In this case, $\Phi(J)$ is the deflection angle corresponding to the angular momentum $J$. It can be observed that Eq. (5) is a coherent sum of different angular momenta. The degree of coherence is connected to the ratio $\gamma=\Gamma/\hbar\omega$, where $\omega$ is the average angular velocity of the intermediate system. A detailed derivation of expression (5) can be obtained in Ref. [27].

In this work, expression (5) is evaluated by means of a Monte Carlo procedure. In this case, the NEAF can be obtained directly from the simulation in the same way as it is done for the experimental data. The partial amplitudes $|\gamma_{\alpha,\mu}|$ are random numbers generated according to a Gaussian distribution with zero average. The energy levels $E_\mu(J)$ are obtained through a sequence of levels spaced by $D_{\mu,\mu+1}$, which are calculated under the assumption that the Hamiltonian random matrix elements are described by the Gaussian orthogonal ensemble statistics [36].

One important advantage of this method is the fact that we can compare theoretical results with experimental ones taking into account the distortions produced by the FRD errors. Another important point to consider in this method is the fact that avoiding simplifications necessary to perform analytical calculations makes more evident the spontaneous spread of the wave packet describing the coherent rotation of the intermediate system. This spontaneous spread of the wave packet becomes prominent in a time interval $\delta t(fm)\sim(\hbar c/4\pi\hbar\omega\Delta^2)\overline{J}$, where $\overline{J}$, $\omega$, and $\Delta$ represent the average

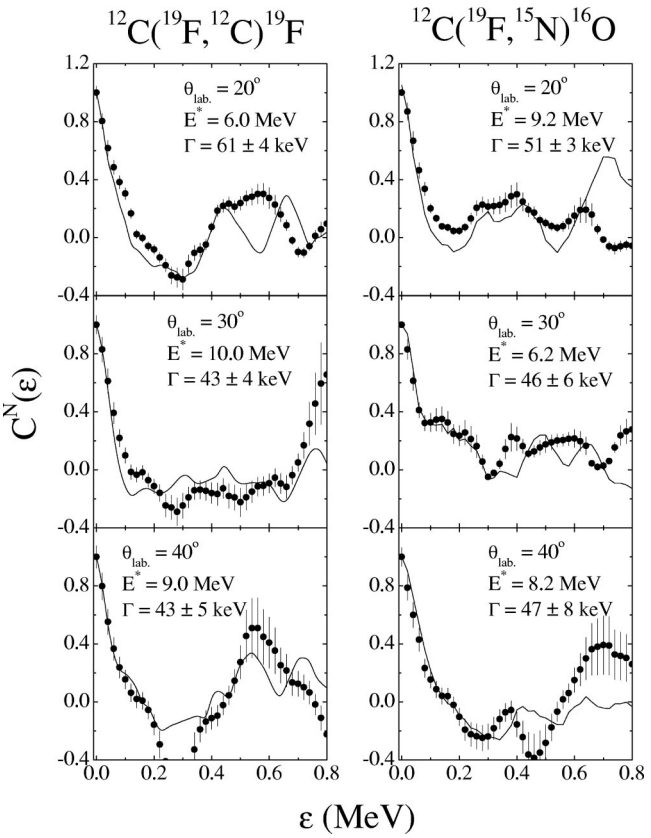


FIG. 9. NEAF for the $^{19}F+^{12}C$ system corresponding to the $^{12}C+^{19}F$ (left) and the $^{15}N+^{16}O$ (right) decay channels in different detection angles and excitation energies. The lines show simulations based on POMLM theory with the parameters in Table II.

value of the total angular momentum, the average angular velocity and the initial dispersion of the wave packet. This effect becomes important in the case of a long lived intermediate state when compared to its rotation time.

In Table II the POMLM parameters used to describe the experimental NEAF are shown. The procedure to find the better parameters is a little bit complex and involves a lot of steps. In order to minimize the number of free parameters some estimations were made. Because we are interested to describe binary processes where the mass assymetry of the fragments is small, the average angular momentum involved in these processes should be close to the critical one. In order to estimate the average angular momentum and its standard deviation, we used a simple compound-nucleus decay model [37] that calculates the cross section as a function of the relative angular momentum of the final fragments assuming a compound-nucleus decay. From the same distribution it is possible to estimate the angular momentum spread $\Delta$. These parameters were kept fixed during the fit procedure and their uncertainties were estimated by varying model parameters (level density parameters, critical angular momentum, and shape of the compound nucleus) inside the systematics for compound nuclei in this mass region.

The phase shift $\Phi$ was initially set as the same as the grazing angle for the systems studied in this work and the elastic scattering angular distributions at $\theta_{c.m.} < 90°$ were

TABLE II. Parameters used to perform POMLM calculations. (*) corresponds to large energy step measurements and (**) corresponds to small energy step measurements.

| Reaction | $\Gamma$ (keV) $\pm 20\%$ | $\hbar\omega$ (keV) $\pm 20\%$ | $\Phi$ $\pm 10\%$ | $\Delta$ $\pm 10\%$ | $\overline{J}(\hbar)$ $\pm 2$ |
|---|---|---|---|---|---|
| $^{10}B(^{16}O,^{16}O)^{10}B$ (*) | 420.0 | 2200 | 22.0 | 4.0 | 14 |
| $^{10}B(^{16}O,^{12}C)^{14}N$ (*) | 250.0 | 2200 | 22.0 | 4.0 | 14 |
| $^{10}B(^{16}O,^{16}O)^{10}B$ (**) | 25.0 | 2200 | 22.0 | 4.0 | 14 |
| $^{10}B(^{16}O,^{12}C)^{14}N$ (**) | 25.0 | 2200 | 22.0 | 4.0 | 14 |
| $^{12}C(^{19}F,^{19}F)^{12}C$ | 45.0 | 2080 | 31.0 | 3.0 | 16 |
| $^{12}C(^{19}F,^{16}O)^{15}N$ | 45.0 | 2080 | 31.0 | 3.0 | 16 |

used to perform a better estimation of this. In this angular region, the elastic scattering is strongly dominated by a very fast process and, in this case, the parameters that contribute most to the shape of the angular distribution are the phase shift and $\gamma$. In this case, $\gamma$ should be very large to describe the very fast falloff of the cross section in this angular region. Once this parameter is obtained it was kept constant. The fit of the angular distributions is described latter in this paper.

The angular velocity $\omega$ was initially set supposing a highly deformed intermediate system (like barbells) with angular momentum $\overline{J}$. This shape can be used to describe a quasimolecular intermediate system where the overlap between target and projectile is small but the system remains bound long enough to exchange mass. This shape can also be used to describe a highly deformed compound nucleus that prefers to decay via a fission mechanism. For the $^{16}O+^{10}B$ system this parameter is set free to fit the elastic scattering NEAF for the large energy step. For the $^{19}F+^{12}C$ system this parameter is kept constant because there is no measurement with large energy steps and, in that case, the NEAF is not sensitive enough to this parameter. The average level width $\Gamma$ is also set free during the fit procedure but it is constrained to only one value for each decay channel. In Fig. 6 we show the elastic scattering NEAF for the $^{16}O+^{10}B$ system for the large energy step measurements. The solid lines are fits using POMLM predictions with the parameters of Table II. The good agreement between the data and the prediction is noticeable. In the case of $\theta_{c.m.}=120°$ there is a bump at $\varepsilon = 2$ MeV in the experimental NEAF as well in POMLM prediction, which can be related to the coherent rotation of the intermediate system. However, because this structure is not well defined in the other NEAF and fluctuations due to FRD are significant at these values of $\varepsilon$, it is not possible to make a strong argument about it. Figure 10 shows simulations computed for different values of $\hbar\omega$ and $\Gamma$. Solid lines represent calculations obtained from the fit of the experimental NEAF, while dotted and dashed lines show calculations where one of the parameters ($\hbar\omega$ and $\Gamma$) is changed by 20%. These simulations were used to estimate the uncertainties on these parameters.

Figures 7–9 show the experimental NEAF for both systems and for the small energy steps. The solid lines correspond to POMLM calculations where the only free param-

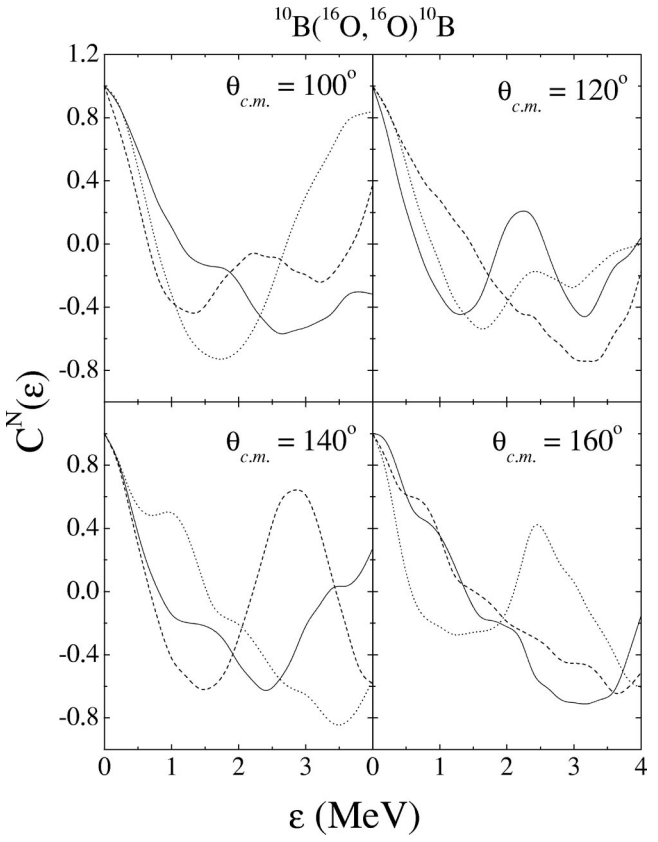


FIG. 10. NEAF simulated for the large step elastic scattering of $^{16}O+^{10}B$ system for different detection angles. Solid lines represent the calculation obtained from the fit of experimental NEAF while dotted lines show calculations where $\hbar\omega$ is reduced by 20% and dashed lines show calculations where $\Gamma$ is reduced by 20%. These simulations were used to estimate the uncertainties on the fit parameters.

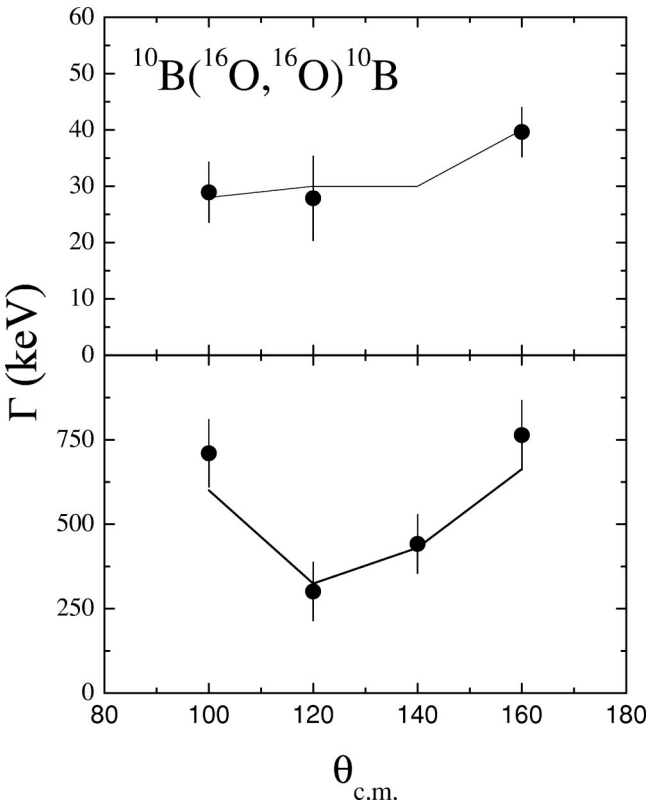


FIG. 11. Elastic scattering widths obtained from the NEAF as a function of the scattering angle for the $^{16}O+^{10}B$ system both for the small (upper) and large (bottom) energy step measurements. The lines correspond to predictions from the POMLM theory.

eter is $\Gamma$. In some cases strong oscillations at large $\varepsilon$ can be observed. These oscillations are mostly due to the finite range of data.

Figure 11 shows the experimental decay width $\Gamma$ of the elastic scattering channel for the $^{16}O+^{10}B$ system for the small and large energy step measurements. The solid lines are calculations using POMLM and there is a good agreement between the data and the model. In the case of the large step measurement, the model describes very well the angular dependence of the experimental width. However, this dependence does not mean different time scales, as the real decay width does not depend on the scattering angle. It comes from the fact that the decay time $(\hbar/\Gamma)$ is close to the rotation time $(2\pi/\omega)$, which creates an interference on the NEAF giving the impression of an angular dependence of the time scale. This angular dependence is not present in the case of the small energy step measurement where the measured decay time is much smaller than the rotation time.

Figure 12 shows the experimental decay width $\Gamma$ of the inelastic decay channel $^{12}C+^{14}N$ for the system $^{16}O+^{10}B$ for the small and large energy step measurements. The solid lines refer to calculations using POMLM. In both cases there is no evident dependence of the decay width with the scattering angle and excitation energy, even for the large step measurement. In the latter case, the time scale involved is slower than that observed in the elastic scattering and the interference with the rotation time is minimized. This large time scale can be explained if we imagine that the intermediate system needs to remain bound a little bit longer to allow some mass exchange. In the case of the small energy step, the time scales observed in the elastic scattering and in this inelastic channel are almost the same. This behavior can be related to a completely thermalized system, like a compound nucleus, and the decay channel does not affect the time scale. This behavior will be discussed in detail later in this paper. In Fig. 13, the experimental decay width $\Gamma$ obtained for the $^{19}F+^{12}C$ system for different decay channels and excitation energies is shown.

From the results above it is clear that the binary decay channels for these systems have contributions of two different mechanisms. One of the mechanisms is very fast, with lifetime comparable to the rotation time of the intermediate system while the other mechanism is a very slow process where the intermediate state remains bound for a time long enough to attain a complete thermalization. These two process compete with each other and it is important to determine their relative yields.

Because of the small and large step measurements for the $^{16}O+^{10}B$ system it is possible to estimate the ratio between cross section of the slow and fast processes. It can be done by considering the EAF amplitude with the same energy av-

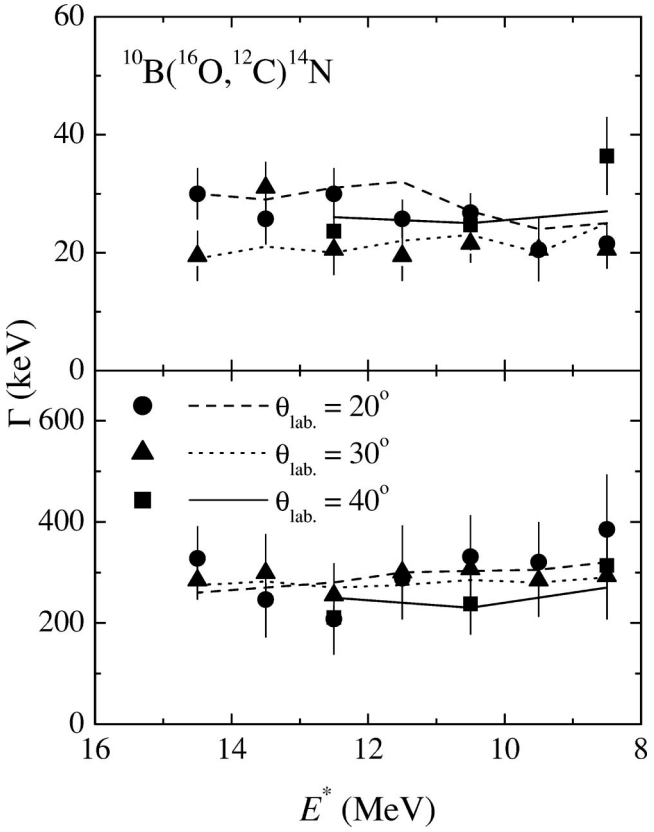


FIG. 12. Experimental widths obtained from the NEAF for the $^{16}O+^{10}B$ system as a function of the fragment excitation energy and angle for the $^{12}C+^{14}N$ decay channel and for the small (upper) and large (bottom) energy step measurements. The lines correspond to predictions from the POMLM theory.

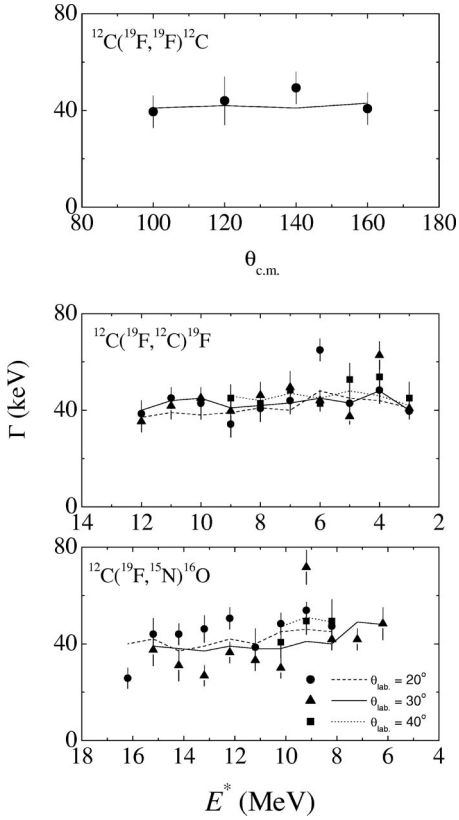


FIG. 13. Experimental widths obtained from NEAF for the $^{19}F+^{12}C$ system for the elastic scattering as a function of the scattering angle (upper). The middle and bottom figures show experimental widths for the $^{12}C+^{19}F$ and $^{15}N+^{16}O$ decay channels as a function of the fragments' excitation energies. The lines show predictions from the POMLM theory.

eraged cross section $\langle\sigma(E,\theta)\rangle$ for both measurements. The EAF amplitude is given by [38]

$$C(0,\theta)=\frac{1}{N_{eff}}\left[1-\left(\frac{\sigma_{gross}}{\langle\sigma\rangle}\right)^2\right], \tag{7}$$

where $N_{eff}$ is the effective number of microscopic channels in the exit channel. $\sigma_{gross}$ is the gross structure cross section and $\langle\sigma\rangle$ is the averaged total cross section. If the total cross section is composed by the sum of the gross and fluctuating cross sections and these processes are incoherent, Eq. (7) becomes

$$C(0,\theta)=\frac{1}{N_{eff}}\frac{\langle\sigma_{fluctuation}\rangle^2}{\langle\sigma\rangle^2}. \tag{8}$$

As the target used to perform the large step measurements is thick enough to wash out the fluctuations due to the slow process, it is possible to write, after some algebraic manipulation, the ratio between the slow and fast cross sections as

$$R=\frac{\langle\sigma_{slow}\rangle}{\langle\sigma_{fast}\rangle}=\sqrt{\frac{C_{s+f}(0,\theta)}{C_f(0,\theta)}-1}, \tag{9}$$

where $C_{s+f}(0,\theta)$ and $C_f(0,\theta)$ are the EAF amplitudes obtained from the small and large step measurements. Figure 14 shows this ratio for the elastic scattering and $^{12}C+^{14}N$ decay channels. The continuous line in Fig. 14(a) is a theoretical prediction based on POMLM, normalized to the data. It is clear that the slow process becomes more important as the scattering angle increases. For the $^{12}C+^{14}N$ decay channel no angular dependence is observed but the slow process dominates the fast one as the fragment excitation energy increases.

In order to double check the set of parameters used to perform the calculations with the POMLM (see Table II), the predictions for the elastic scattering angular distributions were compared to the experimental data. Because of the fact that the range of the angular distributions measured in this work is very limited we used data extracted from the literature [4]. Figure 15 shows the elastic scattering angular distribution for the $^{16}O+^{10}B$ system. The lines show the POMLM predictions. Only the decay width ($\Gamma$) was changed in the calculations to reproduce the behavior due to the shape elastic contribution, and the slow and fast processes measured in this work. The only parameter fitted to the data was the amplitude of the predictions. The angular distribution in the region between 100° and 160° is well reproduced by adding fast and slow processes with the relative weight $R$ determined in Fig. 14(a).

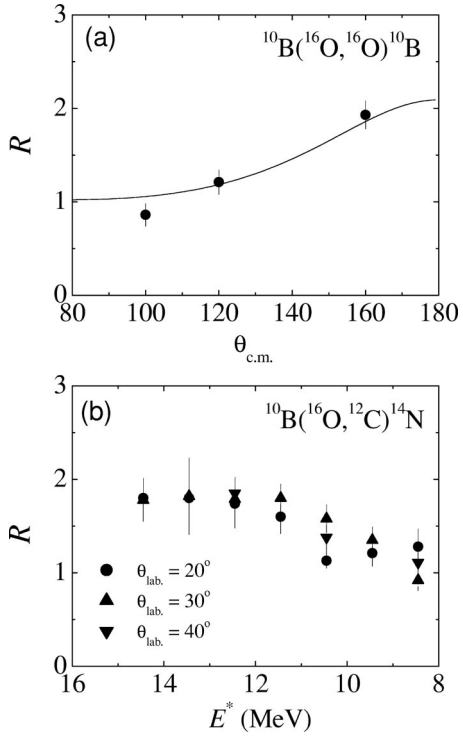


FIG. 14. (a) Ratio between the slow and fast process cross sections for the $^{16}O+^{10}B$ system for the elastic scattering as a function of the scattering angle. (b) The same for the $^{12}C+^{14}N$ decay channel for different angles.

### B. Compound-nucleus predictions

To determine the nature of the widths obtained in the preceding section, we have performed calculations for the total level widths based on compound-nuclei (CN) decay. The relation used for the calculation of the mean level width $\Gamma_{CN}(J)$ at a given angular momentum $J$ is

$$\Gamma_{CN}(J)=\Gamma_{proton}(J)+\Gamma_{neutron}(J)+\Gamma_{\alpha}(J)+\Gamma_{fission}(J). \tag{10}$$

The partial widths for proton, neutron, and $\alpha$ were calculated by [39]

$$\Gamma(J_{CN})=\frac{1}{2\pi\rho_{CN}(E^*_{CN},J_{CN})}\sum_{l=0}^{\infty}\int_0^{\infty}de_{\nu}T_l(e_{\nu}) \times\sum_{s=|J_{CN}-l|}^{J_{CN}+l}\sum_{j_{\nu}=|s-i_{\nu}|}^{s+i_{\nu}}\rho_{\nu}(E^*_{\nu},j_{\nu}) \tag{11}$$

where $E^*_{CN}$ and $J_{CN}$ are the compound-nucleus excitation energy and angular momentum. $E^*_{\nu}$, $j_{\nu}$, and $i_{\nu}$ are the residual excitation energy, angular momentum, and spin. $e_{\nu}$ is the fragments' relative kinetic energy. $\rho_{CN}$ and $\rho_{\nu}$ are the level densities for the compound and residual nucleus, respectively. The fission partial width was computed using the transition state model formalism, and it is given by the sum over all fission partial widths. These widths can be calculated by an equation similar to Eq. (11), where the residual level density is substituted by the system's level density at the saddle point. The transmission coefficients were calculated using a Fermi distribution where the maximum angular momentum for each decay was fixed to $J_{CN}$. The changes of this limit to $J_{CN}/2$ or $J_{CN}/3$ did not cause significant changes to the results. The transmission coefficient's diffusivenesses were taken as 5% of $J_{CN}$. The integration over the kinetic energy was performed in steps of 0.1 MeV. Since we are interested in calculating the total width at high excitation energies (about 15 MeV), no discrete levels were incorporated in this calculation.

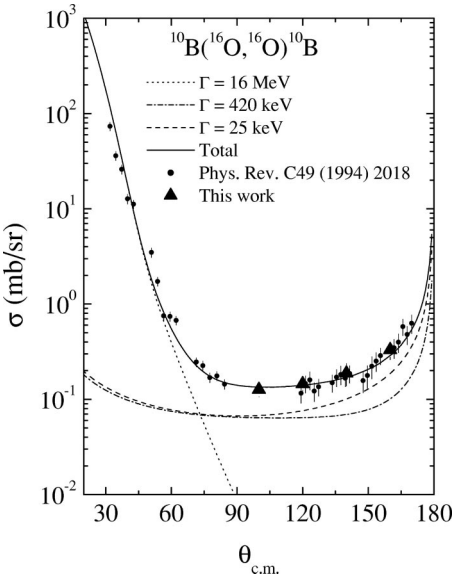


FIG. 15. Elastic scattering angular distribution for the $^{16}O+^{10}B$ system. The triangles show the data obtained in this work and the circles represent data extracted from Ref. [4]. The dotted, dot-dashed, and dashed lines represent the POMLM model predictions with $\Gamma=16$ MeV, $\Gamma=420$ keV, and $\Gamma=25$ keV. The solid line is the total cross section obtained from the incoherent sum of the different predictions.

The level densities are calculated using an angular momentum dependent Fermi gas expression of the form [40]

$$\rho(u,J)=\frac{2J+1}{12}\sqrt{a}\left(\frac{\hbar^2}{2\Im}\right)^{3/2} \times\frac{\exp\left(2\sqrt{a\left[u-\frac{\hbar^2}{2\Im}J(J+1)\right]}\right)}{\left[u-\frac{\hbar^2}{2\Im}J(J+1)\right]^2}, \tag{12}$$

where $a$ is the level density parameter and $\Im$ is the moment of inertia of the rotating system.

The parameters that influence the width calculations the most are the level density parameter $a$ and the moment of inertia $\Im$. Since we are interested in binary processes and the partial waves contributing to these processes are located near the critical value, we assume that a highly deformed compound-nucleus shape is formed and the moment of inertia is written as $\Im=\mu r_0^2(A_1^{1/3}+A_2^{1/3})^2$ (barbells), where $\mu$ is

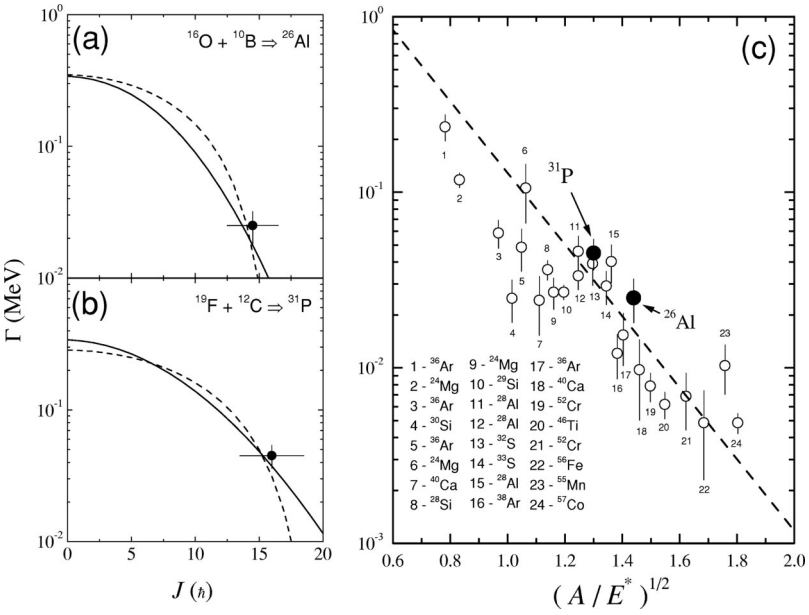


FIG. 16. (a) and (b) are the averaged slow process width as a function of the angular momentum for both measured systems. The solid lines show predictions from Eqs. (10) and (11). Dashed lines correspond to predictions from Eq. (13). (c) Experimentally averaged values inside a systematics obtained from Refs. [42–44]. The dashed line is the empirical calculation from Eq. (13).

the reduced mass. The level density parameter $a$ was taken from a systematics for light nuclei, $a=A/6$.

Another way to calculate the compound-nucleus width is through the use of a semiempirical formula [41]. In this case, the compound-nucleus width is given by

$$\Gamma_{CN}(J)=14\exp\left(-4.69\sqrt{\frac{A_{CN}}{E^{*ef}_{CN}}}\right)\ \text{MeV}, \qquad (13)$$

where $E^{*ef}_{CN}=E^{*}_{CN}-(\hbar^2/2\,\Im)J_{CN}(J_{CN}+1)$ is the intrinsic compound-nucleus excitation energy.

Figures 16(a),(b) show the averaged slow process experimental width as a function of angular momentum. The angular momentum value was calculated from compound nucleus decay predictions for the reaction channels studied in this work. The vertical error bar indicates the mean data deviation and the horizontal error bar indicates the angular momentum window. The solid and dashed lines represent the theoretical calculation from Eqs. (10) and (11) and empirical calculation from Eq. (13). Figure 16(c) shows the experimental average values inside a systematics obtained from Refs. [42–44]. The dashed line, in this case, is the empirical calculation from Eq. (13). It is possible to see a good agreement between the experimental values and compound-nuclei predictions in both cases. These results suggest that the slow process is consistent with the compound-nucleus formation and binary decay, i.e., a fusion-fission process.

Another point to be considered is the relation between the time scales obtained in this work and the intermediate system rotation time. The last one can be calculated considering the moment of inertia and angular momentum calculated above. Figure 17 shows the ratio between the experimental time scales and the rotation time for the $^{12}C+^{14}N$ decay channel of the $^{16}O+^{10}B$ system for the small and large energy step measurements. The solid and dashed lines represent theoretical calculations from Eqs. (10) and (11) and empirical calculation from Eq. (13), respectively. The presence of two different processes is clear. In one of them, the system survives for a long time when compared to the rotation time and this suggests a compound-nucleus decay. In the other process, one has a survival time comparable to the intermediate system rotation time. This suggests the presence of an orbiting mechanism for which the intermediate system does not live a period long enough to equilibrate.

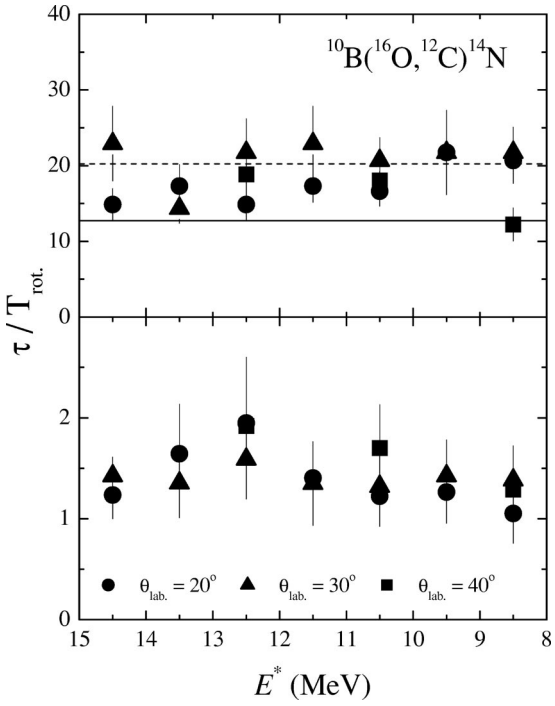


FIG. 17. Ratio between the time scales and the intermediate system rotation time for the $^{12}C+^{14}N$ decay channel of the $^{16}O+^{10}B$ system for the slow (upper) and fast (bottom) processes. The solid line is related to predictions from Eqs. (10) and (11). The dashed line represents predictions from Eq. (13).

## IV. CONCLUSIONS

Fluctuations in the excitation functions of elastic scattering and dissipative binary collisions for the systems $^{16}O+^{10}B$ and $^{19}F+^{12}C$ at $E_{c.m.}\sim 20$ MeV with energy steps of about 25 keV and 200 keV (the latter one only for the system $^{16}O+^{10}B$) have been analyzed. The presence of a very slow process with decay width $\Gamma\sim 30$ keV is evident in both systems. For the system $^{16}O+^{10}B$ it is also evident the presence of a faster process, with time scale comparable to the revolution time of the intermediate state, which is associated to an orbiting process.

The normalized experimental energy autocorrelation functions (NEAF) for both systems were studied in the framework of POMLM. In this analysis it is possible to obtain enough information to characterize the macroscopic intermediate system formed during the reaction, such as average angular momentum, angular velocity, and lifetime. These results suggest that a highly deformed intermediate system is formed and this is in agreement with both the formation of a quasimolecular intermediate state where the system is bound for some time and the formation and decay of a deformed compound nucleus where the lifetime is long enough to allow a complete thermalization of the intermediate system.

For the system $^{16}O+^{10}B$ where the presence of two processes with different time scales is evident it was possible to estimate the relative contribution of each one in the total binary decay yield. In the case of the elastic scattering it is evident that the slow process becomes more important as the scattering angle increases. This behavior can be easily explained in terms of POMLM simulations when we compare the angular distributions for both time scales. For the inelastic channel it is also important to notice that the slow process becomes more important as the excitation energy of the fragments increases.

In order to understand the nature of these processes, decay width predictions based on the formation and binary decay of a compound nucleus were made and compared to the data. The results strongly suggest that the slow process observed in both systems can be related to the fusion-fission mechanism where the compound nucleus, because of the high excitation energy and angular momentum, deforms itself and decays through almost symmetric binary channels.

The fast process observed in the $^{16}O+^{10}B$ system can be be related to the formation of an intermediate quasimolecular system with time scale comparable to its revolution time. This time scale permits some mass exchange but it is not long enough for a complete thermalization and formation of a compound-nucleus-like system. In the case of the elastic scattering channel, it was also noticed the presence of a structure in the NEAF at $\varepsilon=2$ MeV that can be related to the observation of the coherent rotation of the dinuclear system but no strong argument can be made in this case because of the presence of strong oscillations in the NEAF at large $\varepsilon$ due to the finite data range of our measurement.

It is interesting to mention that we have also performed complementary measurements of time scales for the sequential decay of compound nuclei through the utilization of a technique based on the analysis of particle-particle correlations at small relative momenta [45]. In this case, the time scales are related to the sequential decay of the compound nuclei. Even knowing that both techniques concentrate on different stages of the intermediate system decay, it is possible to compare both methods by choosing the systems to be studied in such a way that, for some decay channels, the second decay step of the compound system is the same as the intermediate states studied in this work. In this case, the results obtained are consistent, suggesting that after the first emission, the daughter system is allowed to reequilibrate before the following decay. A detailed comparison between the results obtained by both methods will be presented elsewhere.

## ACKNOWLEDGMENTS

This work was supported in part by Fundação de Amparo à Pesquisa do Estado de São Paulo (FAPESP), Brazil, and Conselho Nacional de Desenvolvimento Científico e Tecnológico (CNPq), Brazil.

[1] D. Shapira, J. L. C. Ford, Jr., J. Gomes del Campo, R. G. Stokstad, and R. M. DeVries, Phys. Rev. Lett. **43**, 1781 (1979).
[2] A. Ray, S. Gil, M. Khandaker, D. D. Leach, D. K. Lock, and R. Vandenbosch, Phys. Rev. C **31**, 1573 (1985).
[3] S. J. Sanders *et al.*, Phys. Rev. Lett. **59**, 2856 (1987).
[4] R. M. dos Anjos, N. Added, N. Carlin, L. Fante, Jr., M. C. S. Figueira, R. Matheus, E. M. Szanto, C. Tenreiro, A. Szanto de Toledo, and S. J. Sanders, Phys. Rev. C **49**, 2018 (1994).
[5] C. Bhattacharya *et al.*, Phys. Rev. C **44**, 1049 (1991).
[6] C. Bhattacharya *et al.*, Phys. Rev. C **52**, 798 (1995).
[7] C. Bhattacharya *et al.*, Phys. Rev. C **54**, 3099 (1996).
[8] D. Shapira, D. DiGregorio, J. Gomes del Campo, R. A. Dayras, J. L. C. Ford, Jr., A. H. Snell, P. H. Stelson, R. G. Stokstad, and F. Pougheon, Phys. Rev. C **28**, 1148 (1983).
[9] P. Braun-Munzinger and J. Barrette, Phys. Rep. **87**, 209 (1982).
[10] W. Von Oertzen and H. G. Bohlen, Phys. Rep., Phys. Lett. **19C**, 1 (1975).
[11] B. Shivakumar, D. Shapira, P. H. Stelson, S. Ayik, B. A. Harmon, K. Teh, and D. A. Bromley, Phys. Rev. C **37**, 652 (1988).
[12] S. Ayik, D. Shapira, and B. Shivakumar, Phys. Rev. C **38**, 2610 (1988).
[13] B. Shivakumar *et al.*, Phys. Rev. C **35**, 1730 (1987).
[14] D. Shapira *et al.*, Phys. Lett. **114B**, 111 (1982).
[15] B. Shivakumar *et al.*, Phys. Rev. Lett. **57**, 1211 (1986).
[16] W. Dunnweber *et al.*, Phys. Rev. Lett. **61**, 927 (1988).
[17] C. Beck *et al.*, Z. Phys. A **334**, 521 (1989).
[18] A. Ray *et al.*, Phys. Rev. C **44**, 514 (1991).
[19] T. Ericson, Phys. Rev. Lett. **5**, 430 (1960).
[20] T. Ericson, Adv. Phys. **9**, 425 (1960).
[21] A. De Rosa *et al.*, Phys. Lett. **160B**, 239 (1985).

[22] G. Pappalardo, Nucl. Phys. **A488**, 395c (1988).
[23] T. Suomijarvi *et al.*, Phys. Rev. C **36**, 181 (1987).
[24] M. C. Mermaz *et al.*, Nucl. Phys. **A456**, 186 (1986).
[25] G. Cardella *et al.*, Z. Phys. A **336**, A387 (1990).
[26] M. Papa, Ph.D. thesis, Catania University, 1994.
[27] M. Papa *et al.*, Phys. Rev. C **61**, 044614 (2000).
[28] M. M. de Moura, A. A. P. Suaide, E. E. Alonso, F. A. Souza, R. J. Fujii, O. B. de Morais, E. M. Szanto, A. Szanto de Toledo, and N. Carlin, Nucl. Instrum. Methods Phys. Res. A **471**, 368 (2001).
[29] R. Cabezas, E. M. Szanto, N. Carlin, N. Added, A. A. P. Suaide, M. M. de Moura, M. G. Munhoz, R. Liguori Neto, J. Takahashi, R. M. dos Anjos, W. H. Z. Cardenas, and A. Szanto de Toledo, Phys. Rev. C **60**, 067602 (1999).
[30] A. A. P. Suaide, Ph.D. thesis, Universidade de São Paulo, 1999.
[31] S. Yu Kun, M. Papa, and D. K. Sunko, Phys. Lett. B **249**, 1 (1990).
[32] S. Yu Kun, Phys. Lett. B **257**, 247 (1991).
[33] S. Yu Kun, M. Papa, and A. B. Robson, Z. Phys. A **347**, 123 (1993).
[34] G. Cardella, M. Papa, G. Pappalardo, F. Rizzo, A. De Rosa, G. Inglima, and M. Sandoli, Z. Phys. A **332**, 195 (1989).
[35] A. De Rosa *et al.*, Phys. Rev. C **44**, 747 (1991).
[36] C. E. Porter, *Statistical Theories of Spectra Fluctuations* (Academic, New York, 1965).
[37] R. G. Stokstad, computer code STATIS (Wright Nuclear Structure Laboratory, Yale University, 1972).
[38] T. Ericson and T. Mayer-Kuckuk, Annu. Rev. Nucl. Sci. **16**, 183 (1966).
[39] K. A. Eberhard, P. Von Bretano, M. Böhning, and P. O. Stephen, Nucl. Phys. **A125**, 673 (1969).
[40] A. Bohr and B. R. Mottelson, *Nuclear Structure* (Benjamin, New York, 1981).
[41] R. Sigh, K. A. Eberhard, and R. G. Stockstad, Phys. Rev. C **22**, 1971 (1980).
[42] M. L. Halbert *et al.*, Phys. Rev. **162**, 899 (1967).
[43] A. N. Behkami and S. I. Najafi, J. Phys. G **6**, 685 (1980).
[44] J. M. Casandjian *et al.*, Phys. Lett. B **430**, 43 (1998).
[45] M. M. de Moura, A. A. P. Suaide, N. Added, E. E. Alonso, W. H. Z. Cardenas, R. J. Fujii, M. G. Munhoz, F. A. Souza, E. M. Szanto, A. Szanto de Toledo, J. Takahasi, N. Carlin, and N. N. Ajitanand, Nucl. Phys. **A696**, 64 (2001).